buildings

MDPI

Article

Cyclic Performance of Reinforced Concrete Columns Strengthened with Basalt-Fibre-Reinforced Cementitious Matrix (BFRCM)

Chellappandian Rajendra Prasath [1,*], Chandrasekaran Jayaguru [2] and Nakarajan Arunachelam [3]

[1] Velammal College of Engineering and Technology, Madurai 625009, India
[2] PSNA College of Engineering and Technology, Dindigul 624622, India; cjayaguru@psnacet.edu.in
[3] Mepco Schlenk Engineering College, Sivakasi 626005, India; arunachelam.n@mepcoeng.ac.in
* Correspondence: crp@vcet.ac.in

Abstract: The purpose of this experimental investigation was to confirm whether the Basalt-Fibre-Reinforced Cement Matrix (BFRCM) effectively enhances the cyclic performance of columns made of reinforced concrete (RC). The BFRCM system, which comprises basalt fabric mesh reinforced with a cementitious matrix containing polyvinyl alcohol (PVA) fibre, has significant practical implications. In the testing phase, concrete and steel reinforcement were used to create RC column specimens, which were then strengthened with three, four, and five layers of BFRCM. The horizontal cyclic and constant axial loads were applied and tested to evaluate the performance of RC columns with and without strengthening. By improving the energy dissipation by approximately 9 to 32% and increasing stiffness by roughly 24 to 44%, the column specimen with three, four, and five layers of BFRCM performed better than the control specimen. Furthermore, incorporating short fibre into the matrix effectively improved the tensile properties of the FRCM systems and decreased the shrinkage-induced cracks. The increased stiffness indicates that the column with BFRCM has better structural strength because it can sustain higher loads with less deflection. The thorough comparative analyses examined the RC column specimens' failure modes, hysteretic responses, stiffness degradation, and energy dissipation, providing a reliable basis for the conclusions. The test results confirmed that the BFRCM effectively enhanced the seismic capabilities and has been promised a way to strengthen RC elements, providing valuable insights for civil engineering and materials science.

Keywords: basalt fabric; cyclic loading; fabric-reinforced cementitious matrix; reinforced concrete column; cyclic performance; seismic parameters

check for updates

Citation: Prasath, C.R.; Jayaguru, C.; Arunachelam, N. Cyclic Performance of Reinforced Concrete Columns Strengthened with Basalt-Fibre-Reinforced Cementitious Matrix (BFRCM). *Buildings* **2024**, *14*, 3496. https://doi.org/10.3390/buildings14113496

Academic Editor: Yun Gao

Received: 27 September 2024
Revised: 28 October 2024
Accepted: 30 October 2024
Published: 31 October 2024

Copyright: © 2024 by the authors. Licensee MDPI, Basel, Switzerland. This article is an open access article distributed under the terms and conditions of the Creative Commons Attribution (CC BY) license (https://creativecommons.org/licenses/by/4.0/).

1. Introduction

Reinforced concrete (RC) buildings are especially vulnerable to the stresses and deformations induced by earthquakes, which can directly lead to catastrophic failure. Instances of extensive failures of RC buildings and other structures have been documented in various locations, including San Fernando Valley, U.S.A. (1971); Mexico City, Mexico (1985); Kobe, Japan (1995); Bhuj, India (2001); Haiti (2010); and so on. A whole moment-resisting framed building may fail for a variety of reasons, including inadequately sized columns, ineffective reinforcements, and poor detailing [1]. Concrete structures are generally designed with a maintenance-free service life of 50 years. Unfortunately, many of today's structures in urban and coastal regions begin to deteriorate in 20 to 30 years or fewer due to two major factors such as environmental and construction errors. Design standards must be revised to account for the increased magnitudes of recent seismic events due to the increasing intensity of earthquakes brought on by climate change [2]. These updated standards also expose the insufficient seismic capacity of older buildings. Raupach et al. [3] concluded that corrosion of reinforcements has emerged as a significant cause of early deterioration in concrete structures globally, especially near marine environments. These

factors have collectively heightened the vulnerability of existing structures to the rising frequency and intensity of today's earthquakes. This has led engineers and scientists to develop more effective seismic strengthening systems to address the inadequate seismic capacity of existing RC structures.

Initial strengthening involved enlarging sections with reinforced concrete or structural steel jackets. This jacketing method confines structural sections and improves seismic capacity [4]. The extent of cross-sectional enlargement and the jacketing materials used determine the increase in seismic capacity. However, this method reduces usable space, increases self-weight, and is prone to corrosion. FRP composites, which are lightweight and strong, have been studied to replace concrete or steel jackets. FRP layers enhance seismic performance by enclosing the plastic hinge sections of structures [5]. Nonetheless, FRP systems exhibited issues such as the incompatibility of adhesives with concrete and the inability to adhere to wet surfaces. These challenges have motivated researchers to investigate an efficient strengthening system in terms of strength and economy. Over the past few years, researchers have studied a cement-based composite system called the fabric-reinforced cementitious matrix (FRCM), formerly known as textile-reinforced mortar or concrete, to overcome the disadvantages of an epoxy-resin-based binding system [6]. This FRCM system is made by different kinds of fabric meshes such as carbon (CFRCM), glass (GFRCM), Aramid (AFRCM), and basalt (BFRCM), and it has been studied by numerous researchers [7–10].

Triantafillou et al. [11] studied the retrofitting of unreinforced masonry walls, RC slabs, RC columns, and RC beams using FRCM with carbon and glass fibre mesh. The results reveal that this retrofitting enhanced the shear and flexural performance under axial load and seismic excitations. Furthermore, FRCM-strengthened RC elements have been studied to increase their flexural, shear, and load-bearing capabilities [12–15]. Additionally, technical documents such as RILEM Technical Committee 232-TDT, CNR-DT 215/2018, and ACI 549.4-20 [16–18] present valuable insights regarding these composite systems' design, application, and characterization for researchers and engineers.

Ortlepp R. and Ortlepp S. [19] explored the application of FRCM with glass fabric mesh for strengthening aged concrete columns with and without steel reinforcement. Comparing columns to their conventional elements, there was a noticeable 85% increase in load-carrying capacity. Increases in the FRCM layer were found to be an effective means of providing confinement, and this improvement was attributed to the addition of concrete cover. On the other hand, Shi-ping et al. investigated the cyclic performance of a corroded RC column strengthened with a fabric mixture of carbon and alkali-free glass yarns under an aggressive environment. The corroded RC columns have two FRCM layers, enhancing their seismic performance [20]. Manisha Shewale et al. [10] found a 50% to 129% strength improvement for RC columns confined with carbon FRCM. Faleschini et al. [6] suggested that the jacketing of reinforced concrete columns with carbon FRCM displays better confinement and a 20% higher load-carrying capacity when compared to non-strengthened specimens.

According to Al-Salloum et al. [21], the best shear strength range of 36–88% of basalt FRCM is found in one to twelve layers. Gopinath et al. discovered that when RC beams reinforced with five layers of basalt FRCM were subjected to fatigue and monotonic tests, the improved ductile capacity was 162% [22]. Tore et al. investigated the RC columns through sprayed glass-fibre-reinforced concrete jackets with basalt mesh to assess the performance under seismic excitations. The test results showed that the proposed seismic retrofitting method improves seismic performance [23]. In addition, innovative cementitious materials such as polypara-phenylene-benzo-bisthiazole (PBO) FRCM have also been explored for structural strengthening [24].

Basalt fibres have competitive mechanical properties, are globally available, and can be produced with a low energy consumption and lower cost than Aramid and carbon fibres [25,26]. It is well known that basalt rocks can be melted at temperatures between 1500 and 1700 °C to produce basalt fibre. They are created from natural materials without

chemicals, and basalt recycling is safe and more effective than glass fibres. It is non-hazardous, eco-friendly, and mechanically robust [25–28].

Basalt fibres have a higher solubility than glass fibres. They are promising for future inorganic fibre applications because their modulus of elasticity is closer to that of glass fibre than carbon fibre. With an ultimate strain of roughly 2%, they show linear elasticity up to failure [29–31]. Sim et al. [28] examined the possibility of basalt fibre as a reinforcing material for structural concrete elements. With a tensile strength of lower than 1000 MPa, the basalt fibre was roughly 30% stronger than carbon fibre and 60% stronger than high-strength glass (S-glass) fibre. Basalt fabric is preferred for composite reinforcement, especially durability, due to its compatibility with a cement-based matrix [22,32]. In this study, the tensile properties of BFRCM with polyvinyl alcohol (PVA) fibres were improved due to its bridging effect [26]. The cementitious composite incorporates PVA fibre and exhibits better composite performance, as reported by Zheng et al. [12].

Many studies were conducted on RC elements strengthened with glass and carbon-fibre-fabric-mesh-reinforced cementitious matrix systems under different loading conditions. As the authors know, this is the first time RC columns are being reinforced using a cementitious matrix made of PVA fibre and basalt fabric mesh under continuous axial load and cyclic lateral displacement reversals. The BFRCM strengthening method is suggested to enhance the seismic performance of non-comfort RC columns. The structural performance of RC columns reinforced with BFRCM under cyclic load reversal has been examined. In addition, the impact of the various BFRCM layers was assessed by comparing the seismic parameters of stiffness, energy dissipation, the hysteretic curve, and the failure mode with the unreinforced specimen.

2. Materials and Methods

2.1. Details of Test Specimens

For this investigation, RC columns with a 1:3 scale were considered. Figure 1 shows the test models' dimensions and reinforcement, while Figure 2 shows the fabricated RC column. The RC column specimen with a cross-section of 150 mm × 150 mm and a height of 1100 mm was connected to a beam of size 150 mm × 150 mm × 450 mm at its top, and a foundation block of plan size 450 mm × 450 mm with a depth of 200 mm was connected rigidly to its bottom. The top beam was designed rigidly to transfer the cyclic load to the RC column specimen. On the other hand, the bottom foundation block was designed rigidly to anchor the RC column specimen to the testing floor. In this investigation, M20-grade concrete was utilized, and the design mix ratio was 1:1.62:3.02. The cement, fine aggregate, and coarse aggregate with a specific gravity of 3.11, 2.72, and 2.84 were used.

The stress–strain graph of concrete is illustrated in Figure 3a. For the current study, four 10 mm bars were used as longitudinal reinforcement, and two-legged 6 mm stirrups were used as transverse reinforcement of the RC column. The tested strength properties of concrete and steel are enumerated in Table 1. The stress–strain graph of steel is shown in Figure 3b. Four different configurations of RC column specimens were fabricated for this investigation. BFRCM strengthening was implemented after 28 days of curing, as described in Section 2.2. Among these, one column configuration without BFRCM strengthening was designated a control column (CC). Three more configurations were made with BFRCM using three, four, and five layers (CC-3BL, CC-4BL, and CC-5BL). The jackets extended from the base of each column to a height of 1100 mm, covering the entire column section.

Table 1. Mechanical properties of concrete and steel.

Characteristic Parameters	Value
Concrete	
Compressive strength (MPa) at 28 days	28.72 (2.6)
Ultimate strain	0.0035 (1.13)

Table 1. *Cont.*

Characteristic Parameters	Value
Split tensile strength (MPa) at 28 days	4.21 (2.26)
Flexural strength (MPa)	3.25 (2.14)
Modulus of elasticity (GPa)	26.79 (2.21)
Steel	
Ultimate tensile strength (MPa)	583 (25)
Yield tensile strength (MPa)	504 (16)
Elongation (%)	15.72 (0.5)
Modulus of elasticity (GPa)	210 (5)

Note: average values and standard deviations are enclosed in parentheses.

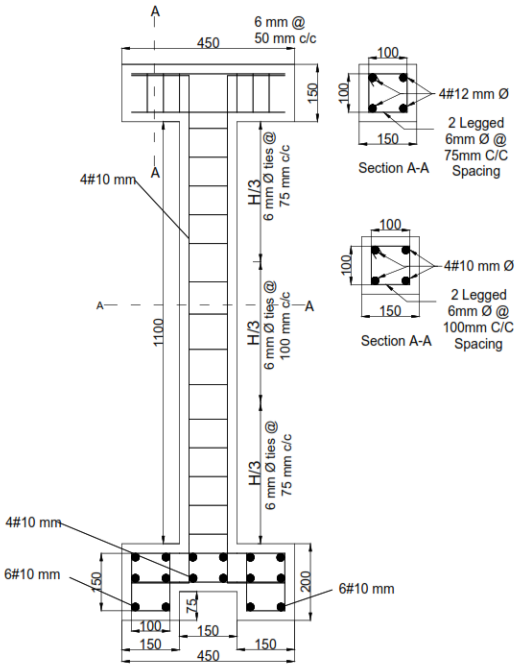


Figure 1. Column geometry and reinforcement details (all dimensions are in mm).



Figure 2. Typical casted RC column specimen.

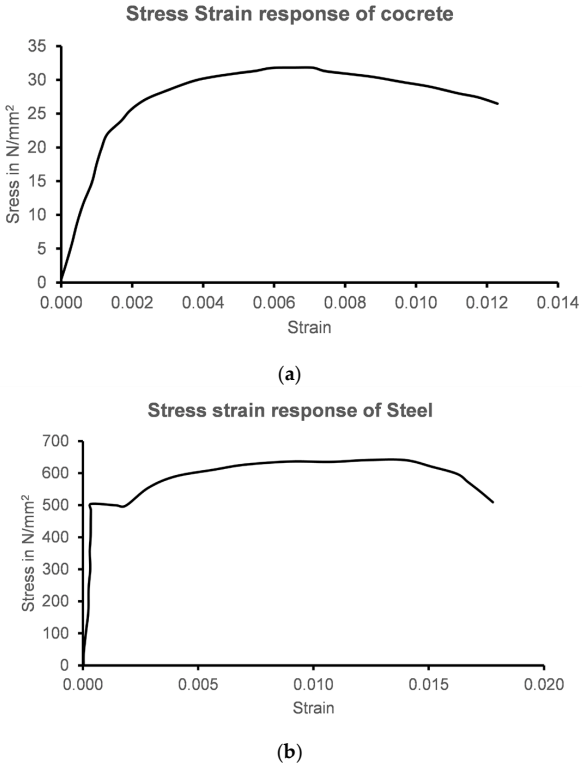


Figure 3. (**a**) Stress–strain response of steel. (**b**) Stress–strain response of concrete.

2.2. Columns Strengthened with BFRCM

The RC column strengthened with BFRCM is depicted in Figure 4, and the BFRCM strengthening process is as follows: The specimen's surface was first roughened and hacked to exhibit assertive bonding behaviour along the entire length of the column region. The columns were wetted with water before being strengthened, and a 5 mm layer of cementitious matrix was applied to them evenly. The fabric mesh was wrapped around the column section after being laid out on a template and coated with the cementitious matrix. A reinforcement layer was completed by spreading the cementitious matrix over the fabric mesh. The previously discussed procedures can be repeated to add reinforcement. During the strengthening process, the basalt fibre bundles were aligned parallel to the stirrup direction, ensuring strong bonding of the BFRP grid without any damage. The cross-section of the columns was slightly increased by using four-sided jacketing. After jacketing, column specimens were cured for 28 days using the gunny bag curing method.



Figure 4. BFRCM-strengthened RC column.

2.3. Basalt Fabric

The production technique of the basalt fibre fabric was distinct. The fabric mesh was made by weaving the fibres with a warp knitting machine and then impregnated with the polymer (such as flexible or rigid polymers) [26]. The technical features of basalt fabric mesh are detailed in Table 2, and Figure 5 illustrates the physical form of basalt fabric mesh.

Table 2. Technical features of basalt fabric.

Specification	Value
Filament density (kg/m^3)	2.65 (0.12)
Specific surface weight (g/m^2)	350 (17.5)
Thickness (mm)	0.70 (0.1)
Tensile strength (kN/m)	70 (3.5)
Elongation at break (%)	2 (0.03)
Modulus of elasticity (GPa)	65 (2.85)
Mesh size (mm)	25 (1.25)

Note: average values and standard deviations are enclosed in parentheses.

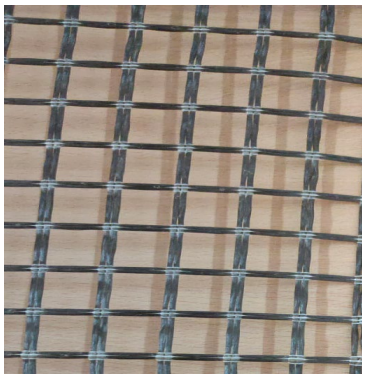


Figure 5. Basalt fabric.

2.4. Cementitious Matrix

A cementitious matrix secures the structural reinforcement meshes of the FRCM composite system [33]. Fibre-reinforced concrete includes synthetic polymers such as glass, steel, and carbon, or natural fibres, to improve mechanical properties and durability [10]. A cement-based material was used as the binder to enrich the composite performance between the concrete and basalt fabric mesh, as stated by Gopinath et al. [22]. The cementitious matrix, composed of ordinary Portland cement (OPC), fly ash, quartz sand, water, superplasticizer, and PVA fibre with a mix proportion (kg/m^3) of 442:840:461:320:5.13:26 with reference from Zheng et al. [12], was considered for this investigation. The short PVA fibre characteristics are shown in Table 3.

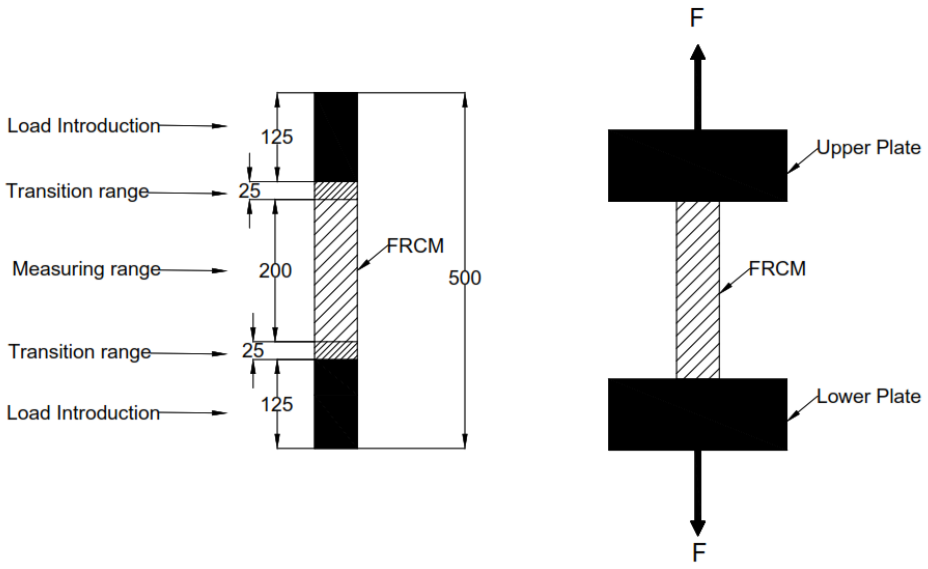
Table 3. Physical features of short PVA fibre.

Length /mm	Diameter /µm	Elastic Modulus /GPa	Tensile Strength /MPa	Elongation /%	Specific Gravity /(g/cm^3)
12	40	40	1600	6	1.14

2.5. Tensile Behaviour of BFRCM

The BFRCM's tensile characteristics were examined as thin plate specimens, and RILEM Technical Committee 232-TDT testing procedures were considered for this investigation [16]. Six specimens per configuration of BFRCM were made and tested with plan dimensions of 500 mm × 60 mm with varying thicknesses of 15, 20, and 25 mm. The specimens were labelled as 3BL, 4BL, and 5BL, which is nothing but three layers, four layers,

and five layers of BFRCM. Tensile testing was performed using a universal testing machine that could support a maximum load of 1000 kN. A displacement rate of 2×10^{-3}/min was used in this tensile test. Figure 6a shows the schematic details of the specimen and tensile strength test setup. The measured deformations of the dial indicator were then connected to the measuring length to determine the strain of the tensile specimen (Figure 6b).



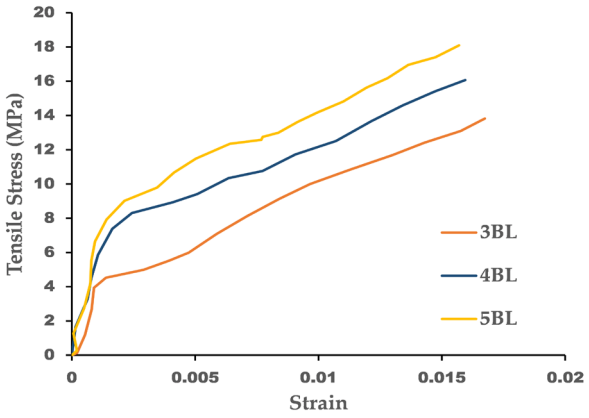
(**a**)



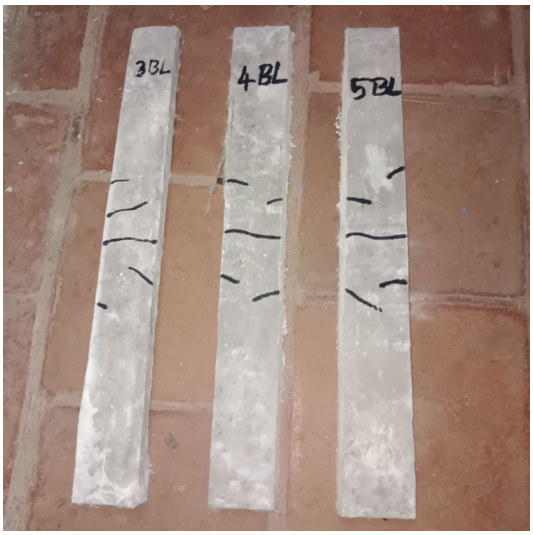
(**b**)

Figure 6. (**a**) Details of FRCM composite specimen and schematic tensile test setup; (**b**) FRCM composite tensile strength test setup.

Short fibres are added to increase the first cracking load, and the bridging effect can enhance the tensile properties of BFRCM [34]. The tensile stress vs. strain curve is shown in Figure 7a, and the failure pattern is shown in Figure 7b. Higher-fabric-ratio specimens had more transverse cracks evenly distributed along the loading direction, improving multi-cracking behaviour [35,36]. Comparable traits found in tested specimens are documented in Figure 7b, and Table 4 provides an overview of the BFRCM's experimental findings. In this investigation, the tensile strengths of 4 BL and 5 BL were greater than that of 3 BL from the perspective of layer comparison.



(**a**)



(**b**)

Figure 7. (**a**) Tensile stress–tensile strain curves; (**b**) Tensile test on coupon specimens with failure pattern.

Table 4. The BGRM's tensile test results.

Specimen ID	Cracking Stress/Mpa	Cracking Strain	Tensile Strength/Mpa	Tensile Strength and Corresponding Strain
3 BL	4.532 (0.29)	0.00139 (0.15)	12.922 (0.74)	0.01595 (0.362)
4 BL	8.304 (0.51)	0.00244 (0.32)	14.872 (1.35)	0.01548 (0.674)
5 BL	9.794 (0.72)	0.00346 (0.58)	18.090 (1.68)	0.01569 (0.931)

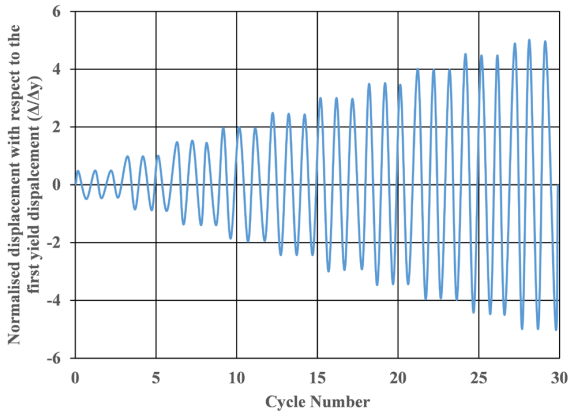
Note: average values and standard deviations are enclosed in parentheses.

2.6. Testing Configuration

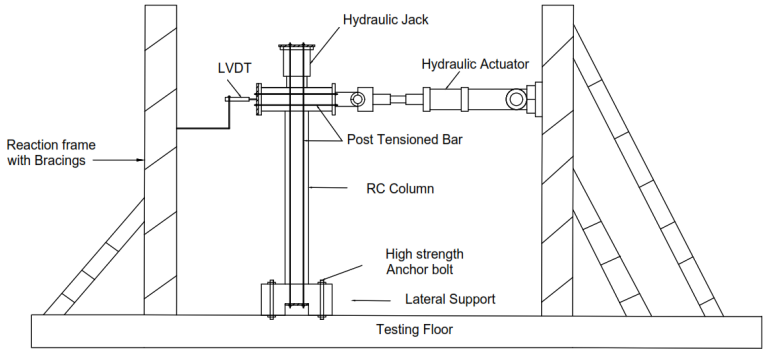
RC columns were tested with constant axial and reverse cyclic lateral loads. A hydraulic jack supplied a continuous axial load with a 0.1 load ratio to simulate the column's dead load. A hydraulic actuator with computerized control from the data acquisition system was generated, and a reversed cyclic lateral load was applied to column specimens. The reaction plates and the high-strength anchor bolts were used to firmly fasten the specimens to the testing floor.

The cyclic behaviour of the RC column was tested using a two-stage loading protocol, as recommended by Paulay et al., Shaingchin et al., Thiruchengode Jothimani V, and Vellalapalayam Guruswamy S [37–39]. In the initial loading phase, three cycles of load control reached the cracking load in both directions, enabling yield displacement assessment. Displacement control was used in subsequent cycles to manipulate specimens so that the

top deflection was integer multiples of the first yield displacement in both directions. Peak load at any set of three cycles dropped to 85% of the absolute maximum load from the previous set, indicating specimen failure. Forces and displacements from load cells and the LVDT (linear variable differential transformer) were recorded continuously until the failure. Figure 8a shows the test programme's loading protocol. The test setup is schematically shown in Figure 8b, and the instrumentation arrangements are shown in Figure 8c. Details of test specimens are listed in Table 5.



(**a**)



(**b**)



(**c**)

Figure 8. (**a**) Loading protocol; (**b**) Schematic test setup; (**c**) Experimental setup of a column with axial and lateral loading.

Table 5. Details of test specimens.

S.No	Specimen ID	Description
1	CC	Control column
2	CC-3BL	CC with three layers of BFRCM of 15 mm thickness
3	CC-4BL	CC with four layers of BFRCM of 20 mm thickness
4	CC-5BL	CC with five layers of BFRCM of 25 mm thickness

3. Experimental Results and Discussion

3.1. Cracking Performance

Figure 9 illustrates the failure characteristics of the four different configurations of RC column specimens. The crack formation and development were consistent for CC-3BL, CC-4BL, and CC-5BL specimens. The specimens remained intact until the elastic stage, as evidenced by the absence of surface cracks during the first load control phase. Horizontal cracks progressively appeared at a height of 152 mm from the column base due to the increase in lateral loading cycles. Horizontal cracks were started at 161 mm, 172 mm, and 178 mm from the base of the column in specimens CC-3BL, CC-4BL, and CC-5BL, respectively. After the first crack appeared, the loading was shifted to displacement control. A crack width microscope (Elcometer 900 concrete crack microscope) with a graduated x50 magnification and internal illumination was employed to measure the width of the cracks. At the point of yielding, the CC, CC-3BL, CC-4BL, and CC-5BL specimens exhibited maximum crack widths of 0.3 mm, 0.25 mm, 0.22 mm, and 0.2 mm, respectively.

With a progressive increase in lateral displacement cycles, the observation of new crack formations and the extension of existing cracks became apparent. Meanwhile, multiple diagonal cracks were generated in the cycle of positive loading and were later closed during the cycle of negative loading. The existing horizontal cracks transitioned to diagonal orientations, while several new diagonal cracks formed as the displacement loading cycles exceeded 1.2Δy, 2.1Δy, 2.3Δy, and 2.5Δy for the respective specimens CC, CC-3BL, CC-4BL, and CC-5BL. As expected, the CC demonstrated more significant cracks with narrower widths, likely due to the higher application of lateral loads. However, the CC-3BL, CC-4BL, and CC-5BL specimens showed fewer cracks, although these cracks were noticeably smaller and narrower than those in the CC specimen. The CC, CC-3BL, CC-4BL, and CC-5BL specimens reached the peak stage at 2.4Δy, 3.0Δy, 3.6Δy, and 3.7Δy, respectively, during the lateral displacement cycles. During the peak phase, crack distribution was measured at 425 mm, 445 mm, 455 mm, and 460 mm from the base of the column along its height for the CC, CC-3BL, CC-4BL, and CC-5BL specimens, respectively.

The CC, CC-3BL, CC-4BL, and CC-5BL specimens reached failure at lateral displacement cycles of 2.75Δy, 3.1Δy, 3.2Δy, and 3.3Δy, respectively. The crack characteristics were consistent among the CC-3BL, CC-4BL, and CC-5BL specimens in the stage of ultimate failure. The distribution of cracks was assessed vertically along the column at positions corresponding to 515 mm, 550 mm, 575 mm, and 640 mm for the CC, CC-3BL, CC-4BL, and CC-5BL specimens, respectively. The CC-4BL and CC-5BL specimens sustained around 85% of the peak lateral force, whereas the CC and CC-3BL specimens tolerated about 80%. This specifies that the CC, CC-3BL, and CC-4BL specimens exhibited a more abrupt decline in lateral force capacity in the failure stage than the CC-5BL specimens. The CC-5BL specimen gradually increased crack formation and propagation, extending over a larger height with narrower cracks. This resulted in enhanced stiffness performance, contributing to resistance against sudden failure. However, while the CC, CC-3BL, and CC-4BL specimens showed fewer cracks, their rapid enlargement in length and width contributed to reduced stiffness properties. This resulted in a sudden reduction in lateral force capacity. At the point of failure, the CC, CC-3BL, CC-4BL, and CC-5BL specimens exhibited maximum crack widths of 3.5 mm, 3.2 mm, 2.8 mm, and 2.6 mm, respectively. The failure modes detected in the CC-3BL, CC-4BL, and CC-5BL specimens were almost similar.

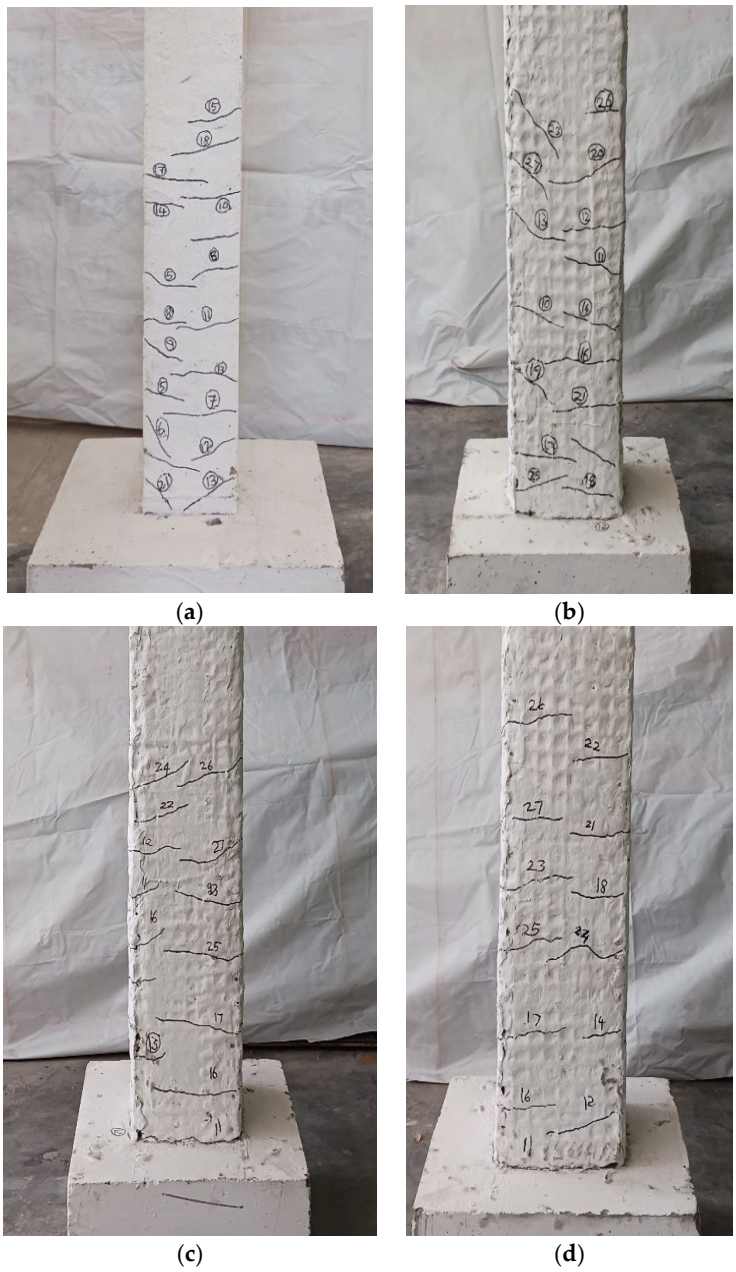


Figure 9. Crack patterns in ultimate-stage specimens of (**a**) CC, (**b**) CC-3BL, (**c**) CC-4BL, and (**d**) CC-5BL.

The predicted tension–flexure failure was validated with these observations. The FRCM jacket protected the core concrete from crushing, which prevented columns from buckling and crushing as confinement action [6,15,40]. Notably, during the seismic tests, no debonding occurred between the matrix layers and basalt fabric reinforcement or between the external jacket and substrate concrete. This demonstrates the excellent bond performance of the proposed composite retrofitting system under significant cyclic displacement reversals [32].

3.2. Lateral Force Versus Displacement Response

The force versus displacement relationship significantly impacts the columns' performance. The applied force against displacement for various column specimens is plotted continuously in Figure 10. Envelope curves are utilized to assess the analysis results of control and BFRCM-strengthened specimens. External confinement increased the flexural strength of low-strength concrete columns during significant deformations. The test obser-

vations exhibited stability and affluence in the forms of the CC-4BL and CC-5BL curves. The lateral force findings for columns in different stages, including the yield, peak, and ultimate stages, are displayed in Table 6.

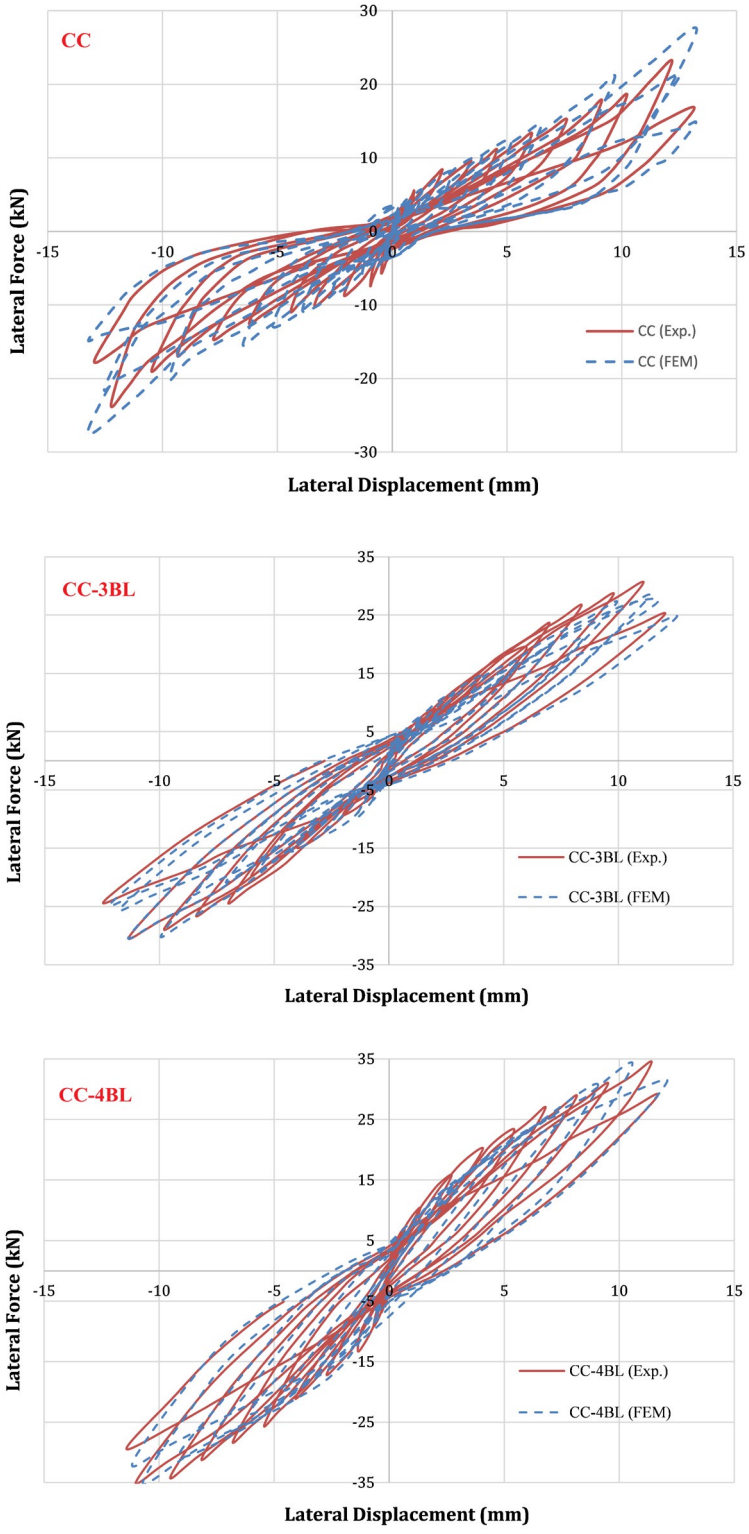


Figure 10. *Cont.*

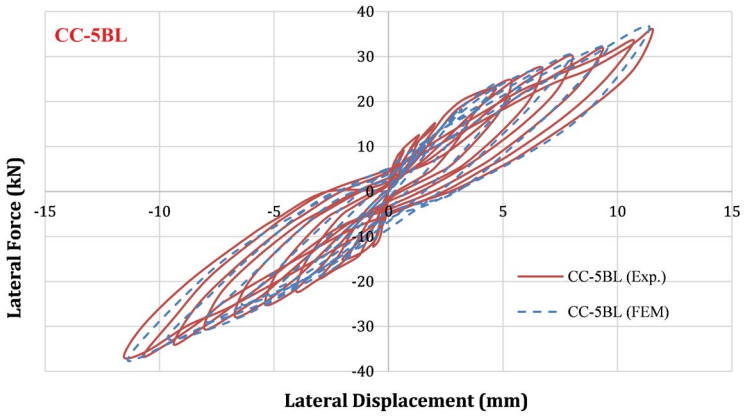


Figure 10. Load displacement envelope for CC, CC 3 BL, CC 4 BL, and CC 5 BL.

Table 6. The experimental findings on lateral force.

Specimen	Crack Deflection Δy (mm)	Crack Load Fy (kN)	Peak Deflection Δp (mm)	Peak Load Fp (kN)	Ultimate Deflection Δu (mm)	Ultimate Load Fu (kN)	Vn ACI (kN)
CC	4.18	11.52	12.86	25.61	13.76	18.87	26.89
CC-3BL	4.00	14.74	11.22	30.51	12.25	24.81	34.18
CC-4BL	4.08	20.66	11.32	34.75	12.32	29.26	42.40
CC-5BL	4.12	21.93	11.55	36.38	12.71	30.94	46.21

A notable pinching effect was observed in the hysteresis loops of CC and CC-3BL. The CC-4BL and CC-5BL curves exhibited stable and abundant shapes. Table 4 presents the lateral force of the columns in the yield, peak, and ultimate stages. The CC-5BL specimen had significantly greater lateral force properties than the other column specimens. The CC-5BL specimen exhibited an increase in yield force by 90% and an increase in peak force by 42% compared to the CC specimen. Compared to the CC specimen, the peak and ultimate displacements of the CC-5BL specimen increased by approximately 10%. This indicates that the CC-5BL specimen exhibited better ductility than the CC specimen. The CC-3BL specimen exhibited an increase in yield force by 28% and an increase in peak force by 19% compared to the CC specimens. The lateral displacement property of the CC-3BL specimen remained largely consistent across all stages. The CC-3BL and CC specimens displayed diminished performance due to an ineffective transverse reinforcement configuration, which could not counteract the pinching effect.

The yield force behaviour of the CC and CC-3BL specimens was almost identical. However, the peak force of the CC-4BL specimen was 10% higher than that of the CC specimen. The lateral displacement of the CC-4BL and CC-5BL specimens saw an increase of approximately 12% and 10% in all stages in comparison to the CC specimen. The BFRCM jacketing configuration of the CC-3BL, CC-4BL, and CC-5BL specimens is vital in enhancing its lateral displacement properties. The CC-3BL, CC-4BL, and CC-5BL specimens exhibited more intensive loops than the CC specimen. At the ultimate phase, approximately 80% of the maximum lateral force was applied to the CC-3BL, CC-4BL, and CC-5BL specimens. This revealed that after reaching the peak load, the load–displacement curves of the CC, CC-3BL, and CC-4BL specimens declined quickly to the failure point. The CC-4BL specimens revealed an increase in yield force and a peak force of 40% and 14% when contrasted with the CC-3BL specimen. Similarly, the yield force and peak force of the CC-5BL specimen were increased by 49% and 19%, respectively, compared to the CC-3BL specimen. In addition, the ultimate force of the CC-4BL and CC-5BL specimens increased by 40% and 14%, respectively, more than the CC-3BL.

The yield force, peak force, ultimate force, yield displacement, peak displacement, and ultimate displacement of CC-4BL were increased by 5% when contrasted with CC-4BL. So, the behaviour of both the CC-4BL and CC-45BL was almost identical. The cementitious matrix and basalt fibre mesh increased displacement ductility, and the strengthened specimens' lateral stiffness showed better confinement action. During cyclic loading, the axial

compression force was concentrated from one side to the other. Therefore, the maximum carrying load capacity was reached at the compression region earlier. The brittle behaviour of the column can then be modified using modern fabric materials with externally confining techniques, which significantly influences the ductile behaviour of low-strength concrete columns. An external jacket subjected to lateral loading can prevent or delay longitudinal bar compression damage from high axial load. Furthermore, Bournas D et al. [15] suggest that in cases of external reinforcement with FRCM, they manage without reducing the lateral load capacity.

3.3. Shear Capacity of RC Columns

3.3.1. RC Columns Without Retrofitting

This study evaluates the nominal shear strength (V_n) of RC columns in their original, non-retrofitted state under the recommendations of [41] as expressed in Equation (1):

$$V_n = V_c + V_s \tag{1}$$

where V_c represents the shear strength contributed by concrete (Equation (2)), and V_s represents the shear strength provided by transverse shear reinforcement in Equation (3):

$$V_c = \frac{1}{6}\left(1 + \frac{P}{14bh}\right) bd\sqrt{f_c'} \tag{2}$$

$$V_s = \frac{A_v f_{yt} d}{s} \tag{3}$$

3.3.2. RC Columns Retrofitted by BFRCM

The assessment of the nominal shear strength (V_n) for RC columns enhanced with BFRCM is expressed in Equation (4):

$$V_n = V_c + V_s + V_f \tag{4}$$

The evaluated nominal shear strength (V_n) for RC columns with BFRCM retrofitting is determined from Equations (5) to (7).

$$V_f = nA_f f_{fv} d_f \tag{5}$$

$$f_{fv} = \varepsilon_{fv} E_f \tag{6}$$

$$\varepsilon_{fv} = \varepsilon_{fu} \leq 0.004 \tag{7}$$

where n represents the number of fabric layers, A_f represents the area of fabric mesh reinforcement, d_f is the effective depth of BFRCM reinforcement, ε_{fv} is the design tensile strain of FRCM, E_f is the tensile elastic modulus of cracked BFRCM, and ε_{fu} denotes the ultimate strain of FRCM.

The total shear strength offered by FRCM reinforcement is to be restricted by Equation (8) [33]:

$$V_f + V_s \leq 0.66\sqrt{f_c'}\, bd \tag{8}$$

3.3.3. Stiffness Degradation

The equivalent elastic modulus and moment of inertia of the column section increased after being strengthened with a UPHC jacket [42]. The specimen's stiffness degradation behaviour was represented by a normalized stiffness (K/K_0), which was obtained by

Equation (9). The initial stiffness was determined as the secant stiffness of the first loading cycle (K_0). Figure 11 illustrates the initial stiffness and stiffness degradation behaviour.

$$K = \frac{|+Pi|+|-Pi|}{|+\Delta i|+|-\Delta i|} \quad (9)$$

where $+Pi$ and $-Pi$ are the peak loads of each positive and negative loading cycle, respectively, and $+\Delta i$ and $-\Delta i$ are the corresponding displacements.

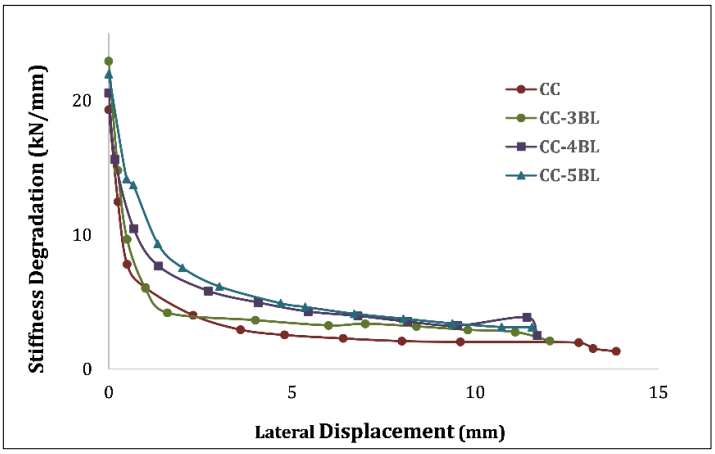


Figure 11. Degradation curve of stiffness.

The prediction of column stiffness characteristics involves utilizing the stiffness properties measured in the initial, yield, peak, and ultimate stages. Table 5 provides the stiffness properties in various stages. The stiffness characteristics of the CC-4BL closely resembled those of the CC-5BL specimen in all loading stages. The CC-5BL specimen exhibited an initial stiffness of 44% higher than that of the CC specimen. Yet, the CC-4BL specimen displayed stiffness properties in yield, peak, and ultimate stages nearly identical to those of the CC-5BL specimen. The CC-4BL specimen displayed an initial stiffness 39% higher than that of the CC specimen. Despite this difference, the CC-5BL specimen demonstrated an equivalent yield stiffness property in comparison to the CC specimen. This specifies that the FRCM configuration helps lessen stiffness degradation, especially during inelastic stages. This behaviour is critical for effective resistance against earthquake forces.

Figure 11 illustrates the stiffness degradation curve, while Table 7 provides the experimental results for stiffness and energy dissipation. Typically, there is a rapid increase in stiffness degradation up to the yield stage, followed by a gradual decrease. As shown in Figure 11, the CC-4BL and CC-5BL specimens displayed a significantly better resistance to stiffness degradation than the CC specimen. Undergoing substantial deformation, the CC-4BL and CC-5BL specimens preserved their lateral strength properties, improving resistance to stiffness degradation. However, the CC and CC-3BL specimens demonstrated pinching characteristics and a significant crack width in their hinge region. Therefore, the CC and CC-3BL specimens exhibit a moderate stiffness performance. The effective positioning of BFRCM is instrumental in preventing abrupt stiffness deterioration, surpassing the efficiency of traditional reinforcement. The columns' well-implemented FRCM configuration and ample confinement enhance the hinge region's stiffness. The CC-4BL and CC-5BL specimens attained improved efficiency in resisting stiffness degradation in all loading stages compared to the CC specimen. A similar finding was also noted in a study conducted by Tong et al. [43], which explored the seismic strengthening of bridge piers using external jacketing with ultra-high-performance fibre-reinforced concrete.

Table 7. Experimental results of stiffness and energy dissipation.

Specimen ID	Initial Stiffness (kN/mm)		Average Initial Stiffness (kN/mm)	Secant Stiffness (kN/mm)	ε_{au} (kN—mm)
	Positive Cycle	Negative Cycle			
CC	6.02	6.23	6.13	1.33	206.60
CC-3BL	7.65	7.61	7.63	2.10	235.31
CC-4BL	8.44	8.59	8.52	2.49	261.68
CC-5BL	8.54	9.14	8.84	2.27	270.86

3.3.4. Energy Dissipation

Integrating the specimens' hysteresis curves can show the energy dissipation, a key parameter for evaluating how well columns resist collapsing under seismic excitations. Figure 12 displays the connections between the cumulative energy dissipation and the specimen loading step. Table 7 illustrates the data on stiffness and energy dissipation capacity. Yield energy dissipation, derived from the area in the hysteresis plot up to the yield stage, is distinct from ultimate energy dissipation, encompassing the total energy dissipated throughout the plot.

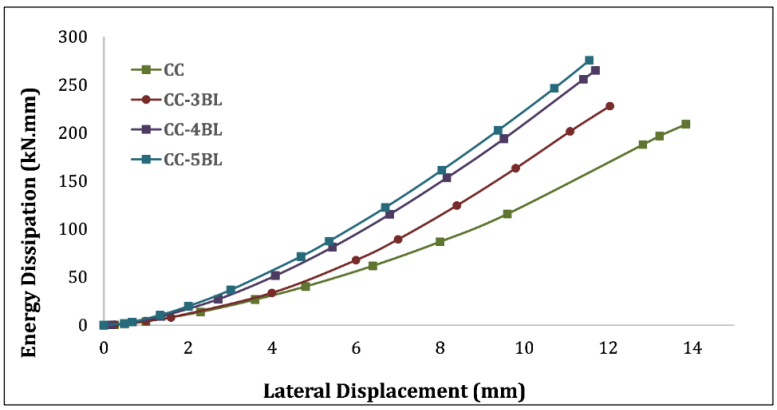


Figure 12. Energy dissipation curve.

Although the CC-3BL, CC-4BL, and CC-5BL specimens showed an energy dissipation capacity performance similar to that of the CC specimen, it demonstrated superior capabilities in both yield energy dissipation and ultimate energy dissipation, boasting an approximately 13%, 26%, and 30% increase compared to the CC specimen. The CC-5BL specimen outperformed the CC specimen with a 31% higher stiffness and 44% higher energy dissipation. While there was a slight increase in ductility for both the CC-4BL and CC-5BL specimens, they exhibited substantial improvements in yield energy dissipation and ultimate energy dissipation capacities. Concrete has become more ductile due to the fibre and cement matrix's capacity to restrict its lateral expansion; the column was further constrained by adding FRCM layers [44].

As previously discussed, the improved lateral displacement characteristics during both elastic and inelastic phases in the CC-4BL and CC-5BL specimens enhance their ductility and energy dissipation performance. This observation specifies that the ductility and energy dissipation properties are enhanced with the effective addition of FRCM to the column specimens [6]. The decreased inelastic response of the CC and CC-3BL specimens influenced their diminished performance in terms of ductility and energy dissipation capacity. The equation for calculating the dissipation of accumulated energy is as follows [39]:

$$E = \sum_{i=1}^{n} \{ [(P_i - P_{i-1}) \times (\Delta_i - \Delta_{i-1}) \times 0.5] + [P_{i-1} \times (\Delta_i - \Delta_{i-1})] \} \quad (10)$$

where P_i and P_{i-1} represent the maximum lateral force at cycle "i" and the previous cycle "$i-1$," respectively, and Δ_i and Δ_{i-1} represent the maximum lateral displacement at cycle "i" and the previous cycle "$i-1$", respectively.

The relationship between cumulative energy dissipation and lateral displacement is presented in Figure 12. All column specimens displayed a uniform energy dissipation pattern, marked by a linear increase in energy dissipation, with notably higher values observed for the CC-4BL and CC-5BL specimens. Compared to CC, the total energy consumption of specimens CC-3BL, CC-4BL, and CC-4BL was higher by 14%, 27%, and 31%, respectively. Figure 12 shows that the CC-4BL and CC-5BL specimens exhibited a higher energy dissipation per cycle than the CC and CC-3BL specimens. Specifically, the CC-5BL specimen demonstrated a superior energy dissipation and better ductility than the other column specimens. The column specimen performed better in elastic and inelastic responses with the aid of the effective FRCM, improving energy dissipation characteristics [32].

3.4. Analytical Investigation

Finite element analysis (FEA) is a computational approach extensively applied in numerous structural challenges to approximate solutions. ANSYS Parametric Design Language 18.0 (APDL) [45] is a nonlinear finite element analysis package that is commercially available and used to perform finite element modelling (FEM). Each element's material geometry and properties were simulated similarly to field test specifications through available material models in the ANSYS element library. The finite element model development process is described as follows: types of elements, material characteristics, loading boundary conditions, connections and meshing.

3.4.1. Materials

The material properties assigned to a part determine its response. Materials can have linear, nonlinear, or temperature-dependent properties depending on their use.

3.4.2. Concrete Model Specifications and Validation

Numerical models were enhanced with the William–Warnke model to accurately represent the observed failure mechanisms in Figure 13a. This allowed for the integration of various material nonlinearities, including cracking, crushing, and plasticity. There are five parameters for this failure surface function. The compressive and tensile meridians are determined using these values. The following five parameters have to be present for establishing the William–Warnke failure surface: ultimate uniaxial tensile strength, ultimate uniaxial compressive strength, ultimate biaxial compressive strength, and shear transfer coefficients for open and closed cracks; their values are expressed in Table 8 [46–48].

Table 8. Properties of concrete.

Properties	Value
Density	2500 kg/m^3
Isotropic elasticity	
Young's modulus	23,585 N/mm^2
Poisson's ratio	0.18
Uniaxial compressive strength	26.7 N/mm^2
Uniaxial tensile strength	3.9 N/mm^2
Biaxial compressive strength	33 N/mm^2
Shear transfer coefficient for crack opening	0.25
Shear transfer coefficient for crack closing	0.75

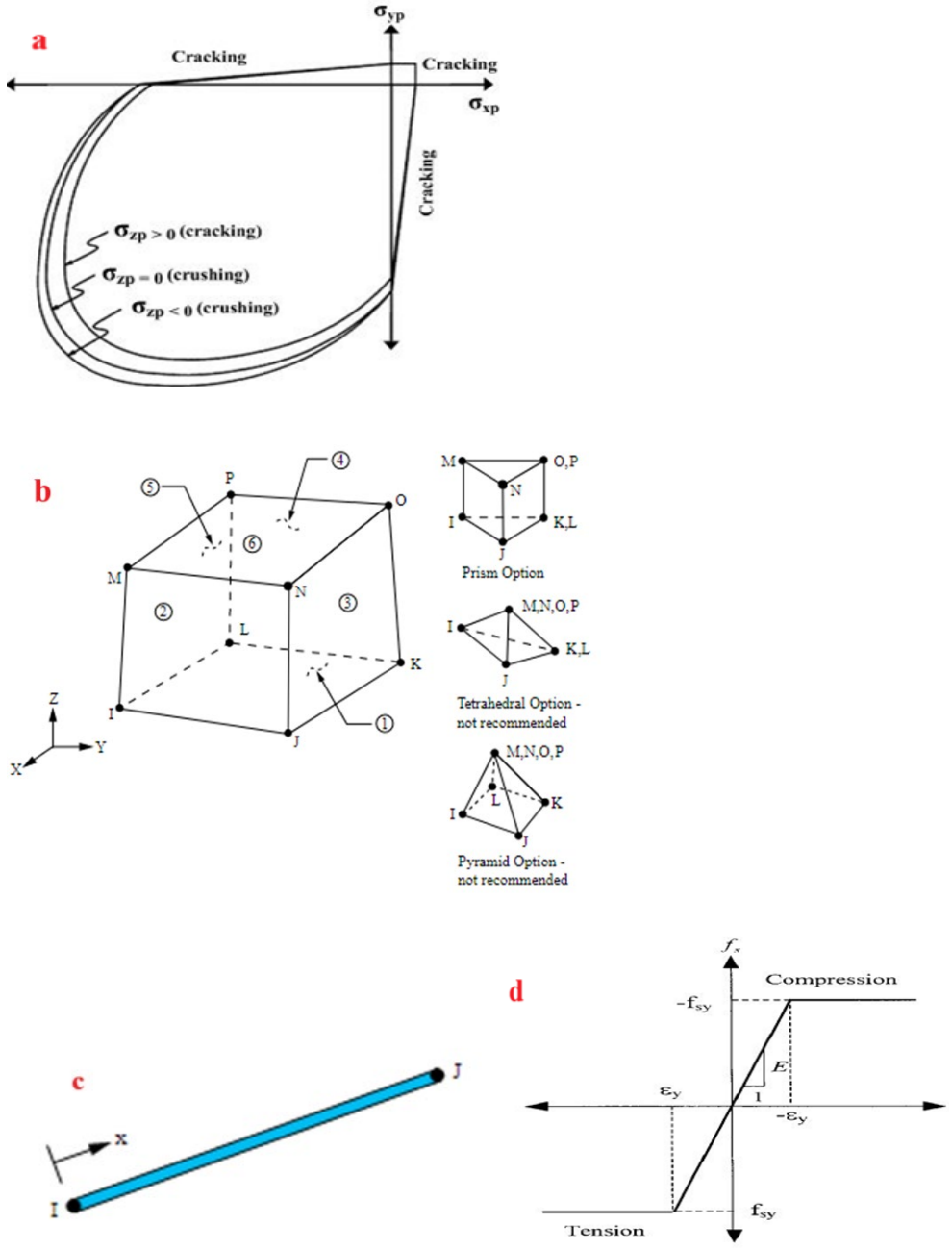


Figure 13. (**a**) William–Warnke model, (**b**) SOLID 185, (**c**) LINK 180, and (**d**) stress–strain model of steel.

3.4.3. Element Types

Figure 13b shows that the SOLID 185 [48] solid model was used to simulate the concrete and BFRCM Layers. It is an eight-nodal element with three degrees of freedom and translation in the nodal x, y, and z directions. The element can simulate plasticity, hyperelasticity, stress stiffening, creep, large deflection, and significant strain capabilities. The concrete and BFRCM properties used in this model are tabulated in Tables 8 and 9.

Table 9. Properties of BFRCM.

Properties	Value
Isotropic elasticity	
Young's modulus	32,787 N/mm^2
Poisson's ratio	0.2
Uniaxial cracking strength	70 N/mm^2
Uniaxial crushing strength	53 N/mm^2
Shear transfer coefficient for crack opening	0.65
Shear transfer coefficient for crack closing	0.3

The LINK 180 [47] element is used to model the steel reinforcement, as illustrated in Figure 13c. This element can exhibit uniaxial tension–compression behaviour with three degrees of freedom in each node and translation in the nodal x, y, and z directions. It includes significant deflection effects and is supported by elasticity, isotropic hardening plasticity, kinematic hardening plasticity, Hill anisotropic plasticity, Chaboche nonlinear hardening plasticity, and creep. Figure 13d shows that a nonlinear material model is used to model the steel reinforcement property, and its material properties are tabulated in Table 10.

Table 10. Properties of steel reinforcement.

Properties	Value
Density	7850 kg/m^3
Isotropic elasticity	
Young's modulus	218,000 N/mm^2
Poisson's ratio	0.3
Bilinear isotropic hardening	
Yield strength	550 N/mm^2
Tangent modulus	20,805 N/mm

3.4.4. Geometry

The RC column geometry was staunchly replicated. The concrete and FRCM jacket models comprise various solid body components. The longitudinal and transverse reinforcements were made of line bodies (Figure 14).

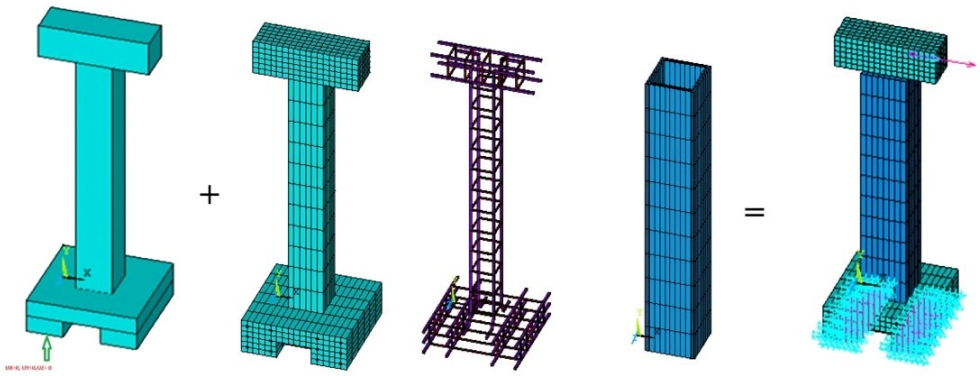


Figure 14. Typical FE model of the RC column with BFRCM.

3.4.5. Connections

The contact area between concrete and FRCM was considered "bonded" for all columns in the current numerical investigation, and sliding or separation between faces or edges was prevented. The bonding between the concrete-to-steel reinforcement and concrete surface of the BFRCM layers was achieved through an inbuilt algorithm in ANSYS called node-to-node merge. Node-to-node contact elements are frequently used when the contact location is known

in advance, and the contact problem involves only a small amount of sliding between the contacting surfaces [49,50]. To ensure a perfect bond, the steel reinforcing link element was connected between the nodes of each adjacent concrete solid element, allowing the two materials to share the same nodes. Hence, combining coincident nodes, a complete bond condition was idealized between the fibre mesh and mortar and between the entire FRCM system and the concrete core, as Ali Hadi Adheem et al. [48] stated. Also, a single fabric layer embedded at the mid-thickness of one mortar layer was used instead of multiple FRCM layers when more than one was used to simplify the analysis.

3.4.6. Mesh

Different mesh sizes were investigated to find a mesh that offers a good balance between accuracy and computational effort (mesh density analysis). The mesh size of 25 mm (for all individual elements of the model) was the most advantageous in offering appropriate accuracy regarding the seismic behaviour of RC columns at an acceptable analysis time, based on the mesh convergence study [48,49]. A mesh size of 100 mm × 25 mm × 25 mm was used for the concrete and steel reinforcement, and 100 mm × 25 mm was considered for BFRCM. The nodes of meshes made for various kinds of materials were combined to display the stresses and strains of these material volumes at a single location.

3.4.7. Boundary Conditions and Loading

The boundary conditions of the experimental investigation were the same as those of the analytical models. All degrees of freedom were limited to establishing a fixed support on the bottom surface of the bottom beam, and the top beam side surface of the column specimens received the reverse cyclic load. A step-by-step amplitude function described the displacement loading cycles [47,49]. An axial force was applied at the top beam, and a step-by-step amplitude function described the displacement loading cycles.

3.4.8. Verification Results

In the failure stage of the column specimens, the total strain energy was analyzed using contour plots of equivalent plastic strain. Figure 15a–d display the plots of equivalent plastic strain for all specimens. The finite element model in ANSYS was utilized to validate the experimental lateral load capacity of the RC column. A comparison of the results from FEA with the experimental findings indicates that the results demonstrate patterns consistent with the experimental data. The FEA effectively captures the nonlinear response of the specimen until the peak stage. This variation may be attributed to the minor differences in the nonlinear material properties of concrete, steel, and BFRCM modelled in the FEA compared to the experimental results, as shown in Table 11.

Table 11. Comparison of experimental and FEA findings.

Specimen ID	Experimental		FEA		Difference (%)	
	Peak Deflection Δp (mm)	Peak Load Fp (kN)	Peak Deflection Δp (mm)	Peak Load Fp (kN)	Deflection Δ (%)	Load F (%)
CC	12.86	25.61	13.26	27.29	3	7
CC-3BL	11.22	28.51	11.36	29.40	1	4
CC-4BL	11.32	34.75	10.64	32.63	5	1
CC-5BL	11.55	36.38	11.39	38.00	1	2

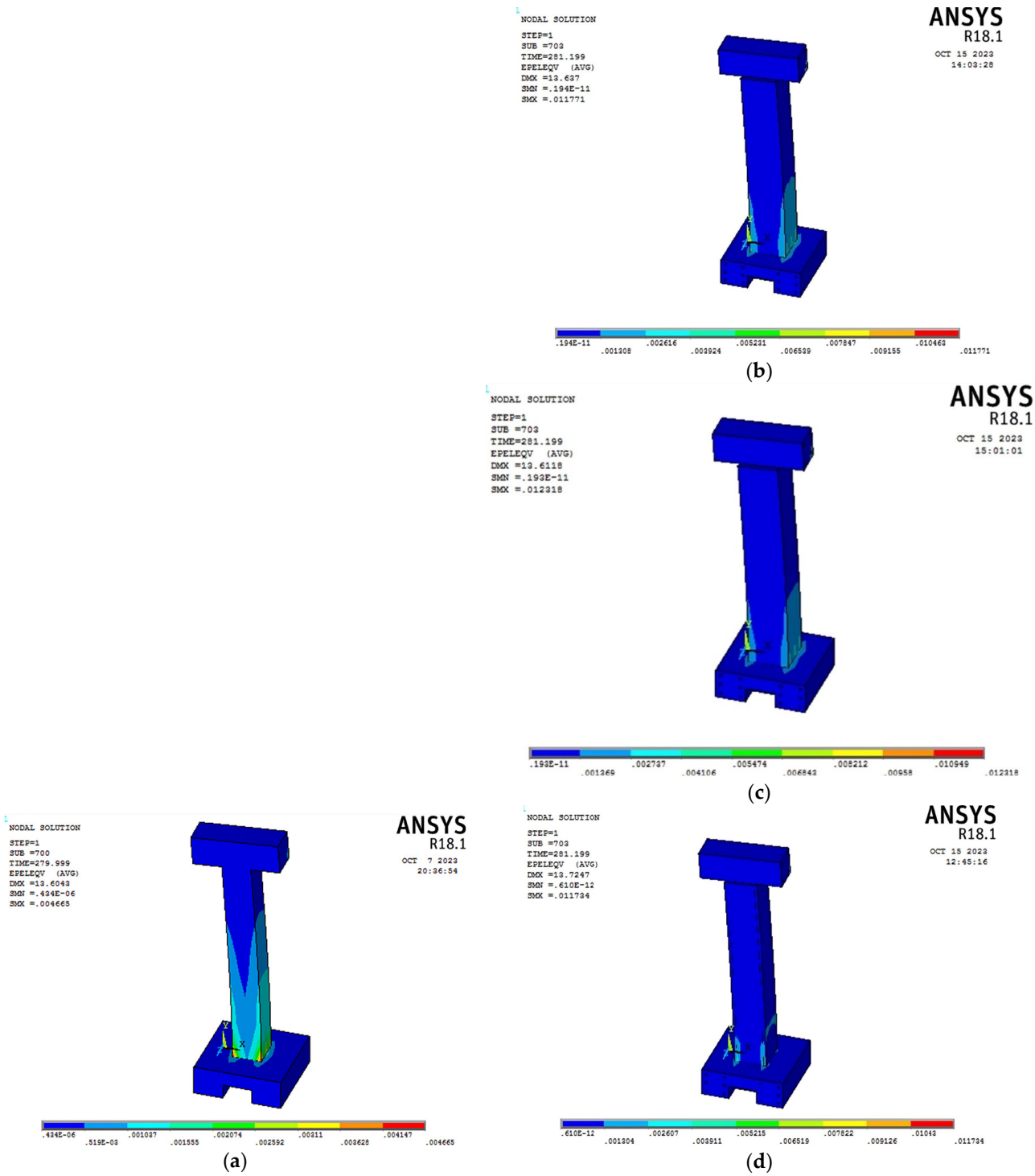


Figure 15. The equivalent plastic strain predicted by FEA: (**a**) CC, (**b**) CC-3BL, (**c**) CC-4BL, and (**d**) CC-5BL.

The difference between the experimental results and the FEA-derived peak load and displacement values was less than 7% for both parameters. There is very little difference between the experimental and numerical values of the ultimate and maximum loads, as well as ultimate displacements (based on the ultimate experimental displacement or experimental load). The RC column with the five-layer BFRCM (CC-5BL) reinforcement configuration outperformed the other specimens, according to the analytical and experimental comparison results.

4. Conclusions

The seismic behaviour and effectiveness of RC columns using three distinct BFRCM strengthening method configurations were evaluated in this study. Combining a matrix reinforced with PVA fibre with basalt fabric mesh improves the advantageous qualities of the composite components. This encompasses the crack resistance and bridging effect in BFRCM. The control and strengthened columns underwent simultaneous testing with axial and lateral cyclic loading in reverse. The main conclusions drawn from this investigation are as follows:

The columns reinforced with BFRCM exhibited superior hysteretic performance and stiffness degradation compared to the control columns. The BFRCM confinement enhanced the RC columns' ductility, stiffness, strength, and energy dissipation, among other seismic properties. With improved energy dissipation and displacement ductility properties, the hysteresis response and ultimate load capacity were enhanced, and there was a notable resistance to stiffness degradation. Furthermore, theoretical analysis was conducted to validate the ultimate load of the experimental and analytical studies, revealing an acceptable level of difference.

These findings demonstrated the superior performance of the RC column with the four- and five-layer BFRCM (CC-4BL and CC-5BL) reinforcement configurations compared to the other specimens. The specimen is more constrained by BFRCM as more reinforcement layers are added. As the number of BFRCM-reinforced layers increases, the ductility of the reinforced specimens is enhanced. This suggests that the structural characteristics of column specimens with more BFRCM layers are superior to those with a lower count.

According to the experimental results, the FRCM strengthening technique is highly effective for seismically deficient RC columns under reverse cyclic and axial loads. Due to its exceptional performance with RC members with low to medium axial load ratios, it is an excellent choice for the recommended strengthening technique.

The effects of basalt fabric mesh with other cementitious materials still need to be thoroughly investigated, although the current study examined a wide range of characteristics.

Author Contributions: Conceptualization, formal analysis, methodology, investigation, data validation: C.R.P. and C.J.; funding: C.R.P.; writing—original draft preparation: C.R.P., C.J. and N.A., writing—review and editing: C.R.P., C.J. and N.A. All authors have read and agreed to the published version of the manuscript.

Funding: This research received no external funding.

Data Availability Statement: Data are available upon request; to those interested, please contact the corresponding author.

Conflicts of Interest: The authors declare no conflicts of interest.

References

1. Murugan, K.; Sengupta, A.K. Seismic Performance of Strengthened Reinforced Concrete Columns. *Structures* **2020**, *27*, 487–505. [CrossRef]
2. Maji, C.; Sadhukhan, B.; Mukherjee, S.; Khutia, S.; Chaudhuri, H. Impact of Climate Change on Seismicity: A Statistical Approach. *Arab. J. Geosci.* **2021**, *14*, 2725. [CrossRef]
3. Raupach, M.; Schieûl, P. Macrocell Sensor Systems for Monitoring of the Corrosion Risk of the Reinforcement in Concrete Structures. *NDTE Int.* **2001**, *34*, 435–442. [CrossRef]
4. Ganesh, P.; Murthy, A.R. Repair, Retrofitting and Rehabilitation Techniques for Strengthening of Reinforced Concrete Beams—A Review. *Adv. Concr. Constr.* **2019**, *8*, 101–117. [CrossRef]
5. *FEMA 547/2006*; Techniques for the Seismic Rehabilitation of Existing Buildings. FEMA: Washington, DC, USA, 2006.
6. Faleschini, F.; Zanini, M.A.; Hofer, L.; Pellegrino, C. Experimental Behavior of Reinforced Concrete Columns Confined with Carbon-FRCM Composites. *Constr. Build. Mater.* **2020**, *243*, 118296. [CrossRef]
7. Dai, J.-G.; Bai, Y.-L.; Teng, J.G. Behavior and Modeling of Concrete Confined with FRP Composites of Large Deformability. *J. Compos. Constr.* **2011**, *15*, 963–973. [CrossRef]
8. Chandra Ray, B.; Rathore, D. A Review on Mechanical Behavior of FRP Composites at Different Loading Speeds. *Crit. Rev. Solid State Mater. Sci.* **2015**, *40*, 119–135. [CrossRef]

9. Venigalla, S.G.; Nabilah, A.B.; Nasir, N.A.M.; Safiee, N.A.; Abd Aziz, F.N.A. Textile-Reinforced Concrete as a Structural Member: A Review. *Buildings* **2022**, *12*, 474. [CrossRef]
10. Shewale, M.; Bahrami, A.; Murthi, P.; Chidambaram, R.S. Enhancing Load-Carrying Capacity of Reinforced Concrete Columns with High Aspect Ratio Using Textile-Reinforced Mortar Systems. *Buildings* **2024**, *14*, 2050. [CrossRef]
11. Triantafillou, T.; Papanicolaou, C. Innovative Applications of Textile-Based Composites in Strengthening and Seismic Retrofitting as Well as in the Prefabrication of New Structures. In *Advanced Materials Research*; Trans Tech Publications: Stafa, Switzerland, 2013; Volume 639–640, pp. 26–41.
12. Zheng, A.; Liu, Z.; Li, F.; Li, S. Experimental Investigation of Corrosion-Damaged RC Beams Strengthened in Flexure with FRP Grid-Reinforced ECC Matrix Composites. *Eng. Struct.* **2021**, *244*, 112779. [CrossRef]
13. Jie, S.; Yin, S.-P.; Fei, W.; YangYang. Experimental Study on the Fatigue Behaviour of RC Beams Strengthened with TRC After Sustained Load Corrosion. *Constr. Build. Mater.* **2017**, *131*, 713–720. [CrossRef]
14. Kim, H.Y.; You, Y.J.; Ryu, G.S.; Koh, K.T.; Ahn, G.H.; Kang, S.H. Flexural Strengthening of Concrete Slab-Type Elements with Textile Reinforced Concrete. *Materials* **2020**, *13*, 2246. [CrossRef] [PubMed]
15. Bournas, D.A.; Lontou, P.V.; Papanicolaou, C.G.; Triantafillou, T.C. Textile-Reinforced Mortar Versus Fiber-Reinforced Polymer Confinement in Reinforced Concrete Columns. *ACI Struct. J.* **2007**, *104*, 740–748. [CrossRef]
16. RILEM Technical Committee 232-TDT (Wolfgang Brameshuber). Recommendation of RILEM TC 232-TDT: Test Methods and Design of Textile Reinforced Concrete: Uniaxial Tensile Test: Test Method to Determine the Load Bearing Behavior of Tensile Specimens Made of Textile Reinforced Concrete. *Mater. Struct. Mater. Constr.* **2016**, *49*, 4923–4927. [CrossRef]
17. *CNR-DT 215/2018*; Guide for the Design and Construction of Externally Bonded Fibre Reinforced Inorganic Matrix Systems for Strengthening Existing Structures. CNR: Rome, Italy, 2020.
18. *ACI 549. 4-20*; Guide to Design and Construction of Externally Bonded Fabric-Reinforced and Steel-Reinforced Grout Systems for Repair and Strengthening of Concrete Structures. ACI: Farmington Hills, MI, USA, 2020.
19. Ortlepp, R.; Ortlepp, S. Textile Reinforced Concrete for Strengthening of RC Columns: A Contribution to Resource Conservation through the Preservation of Structures. *Constr. Build. Mater.* **2017**, *132*, 150–160. [CrossRef]
20. Yin, S.-P.; Hu, X.-Q.; Hua, Y.-T. Study on the Compression Performance of Small Eccentric Degradation Columns Strengthened with TRC in a Chloride Environment. *Constr. Build. Mater.* **2018**, *176*, 50–59. [CrossRef]
21. Al-Salloum, Y.A.; Hussein, M.E.; Elsanadedy, M.; Saleh, H.A.; Alsayed, H.; Iqbal, R.A. Experimental and Numerical Study for the Shear Strengthening of Reinforced Concrete Beams Using Textile-Reinforced Mortar. *J. Compos. Constr.* **2012**, *16*, 74–90. [CrossRef]
22. Gopinath, S.; Murthy, A.R.; Iyer, N.R.; Prabha, M. Behaviour of Reinforced Concrete Beams Strengthened with Basalt Textile Reinforced Concrete. *J. Ind. Text.* **2015**, *44*, 924–933. [CrossRef]
23. Tore, E.; Comert, M.; Demir, C.; ILKI, A. Muhammed Maraşlı Seismic Retrofit of Columns Using Basalt Mesh Reinforced Sprayed GRC Jacket. In *Glass Fibre Reinforced Concrete*; DergiPark: Ankara, Turkey, 2015; pp. 1–7.
24. Mazzuca, P.; Pisani, B.; Firmo, J.P.; Ombres, L. Tensile and Bond Properties at Elevated Temperatures of a PBO-FRCM Composite System for Strengthening Concrete Elements: Experimental and Analytical Investigations. *Constr. Build. Mater.* **2024**, *432*, 136519. [CrossRef]
25. Yao, Y.; Zhu, D.; Zhang, H.; Li, G.; Mobasher, B. Tensile Behaviors of Basalt, Carbon, Glass, and Aramid Fabrics under Various Strain Rates. *J. Mater. Civ. Eng.* **2016**, *28*, 04016081. [CrossRef]
26. Zhang, X.; He, W.; Zhang, Y.; Chen, C.; Wu, X. Tensile Behavior of Basalt-Fiber-Grid-Reinforced Mortar Before and After Exposure to Elevated Temperature. *Buildings* **2022**, *12*, 2269. [CrossRef]
27. Jamshaid, H.; Mishra, R.; Militky, J.; Hussain, S. *Basalt Hybrid Woven Textile Materials for Advanced Thermal Applications*; EBSCO: Ipswich, MA, USA, 2019; Volume 44.
28. Sim, J.; Park, C.; Moon, D.Y. Characteristics of Basalt Fiber as a Strengthening Material for Concrete Structures. *Compos. B Eng.* **2005**, *36*, 504–512. [CrossRef]
29. Dhand, V.; Mittal, G.; Rhee, K.Y.; Park, S.J.; Hui, D. A Short Review on Basalt Fiber Reinforced Polymer Composites. *Compos. B Eng.* **2015**, *73*, 166–180. [CrossRef]
30. John, V.J.; Dharmar, B. Influence of Basalt Fibers on the Mechanical Behavior of Concrete—A Review. *Struct. Concr.* **2021**, *22*, 491–502. [CrossRef]
31. Ludovico, M.D.; Prota, A.; Manfredi, G. Structural Upgrade Using Basalt Fibers for Concrete Confinement. *J. Compos. Constr.* **2010**, *14*, 541–552. [CrossRef]
32. Ates, A.O.; Hajihosseinlou, S.; Nasrinpour, A.; Demir, C.; Comert, M.; Marasli, M.; Ilki, A. Seismic Retrofit of Substandard RC Columns Using Sprayed Glass Fiber-Reinforced Mortar and Basalt Textile Reinforcement. *J. Earthq. Eng.* **2023**, *28*, 1615–1642. [CrossRef]
33. *ACI 549-13*; Guide to Design and Construction of Externally Bonded Fabric-Reinforced Cementitious Matrix (FRCM) Systems for Repair and Strengthening Concrete and Masonry Structures. ACI: Farmington Hills, MI, USA, 2013.
34. Osman Ates, A.; Khoshkholghi, S.; Tore, E.; Marasli, M.; Ilki, A. Sprayed Glass Fiber-Reinforced Mortar with or without Basalt Textile Reinforcement for Jacketing of Low-Strength Concrete Prisms. *J. Compos. Constr.* **2019**, *23*, 04019003. [CrossRef]
35. Cuypers, H.; Wastiels, J. Stochastic Matrix-Cracking Model for Textile Reinforced Cementitious Composites under Tensile Loading. *Mater. Struct. Mater. Constr.* **2006**, *39*, 777–786. [CrossRef]

36. Mobasher, B.; Peled, A.; Pahilajani, J. Distributed Cracking and Stiffness Degradation in Fabric-Cement Composites. *Mater. Struct. Mater. Constr.* **2006**, *39*, 317–331. [CrossRef]
37. Paulay, T.; Priestley, M.J.N.; Synge, A.J. Ductility in Earthquake Resisting Squat Shearwalls. In *ACI Journal Proceedings*; ACI: Farmington Hills, MI, USA, 1982.
38. Shaingchin, S.; Lukkunaprasit, P.; Wood, S.L. Influence of Diagonal Web Reinforcement on Cyclic Behavior of Structural Walls. *Eng. Struct.* **2007**, *29*, 498–510. [CrossRef]
39. Thiruchengode Jothimani, V.; Vellalapalayam Guruswamy, S. Cyclic Performance of RC Shear Wall Embedded with X-Shaped Web Reinforcement. *Arab. J. Sci. Eng.* **2021**, *46*, 4971–4983. [CrossRef]
40. Yin, S.; Yang, Y.; Ye, T.; Li, Y. Experimental Research on Seismic Behavior of Reinforced Concrete Columns Strengthened with TRC under Corrosion Environment. *J. Struct. Eng.* **2017**, *143*, 04016231. [CrossRef]
41. *ACI 318-14*; Building Code Requirements for Structural Concrete Commentary on Building Code Requirements for Structural Concrete. ACI: Farmington Hills, MI, USA, 2014.
42. Zhang, Y.; Yang, J.; Li, T.; Deng, M. Mechanical Behavior of RC Columns Strengthened with Thin UHPC Jacket Under Cyclic Loads. *J. Build. Eng.* **2022**, *49*, 104065. [CrossRef]
43. Tong, T.; Wang, J.; Lei, H.; Liu, Z. UHPC Jacket Retrofitting of Reinforced Concrete Bridge Piers with Low Flexural Reinforcement Ratios: Experimental Investigation and Three-Dimensional Finite Element Modeling. *Struct. Infrastruct. Eng.* **2021**, *17*, 1315–1337. [CrossRef]
44. Zhang, Q.; Yang, Q.C.; Gu, X.L.; Jiang, Y. Study on Axial Compression Properties of Concrete Columns Wrapped with Basalt Textile-Reinforced Fine Concrete (BTRC) Jackets. *Constr. Build. Mater.* **2023**, *363*, 129809. [CrossRef]
45. *ANSYS Mechanical APDL Material Reference*; ANSYS Software Revision 2020R1; ANSYS: Canonsburg, PA, USA, 2020.
46. Willam, K.J.; Warnke, E.P. Constitutive Model for Triaxial Behaviour of Concrete. In Proceedings of the Seminar on Concrete Structures Subject to Triaxial Stresses, International Association of Bridge and Structural Engineering Conference, Bergamo, Italy, 17–19 May 1974.
47. Parvin, A.; Alhusban, M. Lateral Deformation Capacity and Plastic Hinge Length of RC Columns Confined with Textile Reinforced Mortar Jackets. *CivilEng* **2021**, *2*, 670–691. [CrossRef]
48. Adheem, A.H.; Kadhim, M.M.A.; Jawdhari, A.; Fam, A. Confinement Model for Concrete Wrapped with Fiber Reinforced Cementitious Mortar. *Constr. Build. Mater.* **2021**, *312*, 125401. [CrossRef]
49. Anagnostou, E.; Rousakis, T. Performance of Steel Bar Lap Splices at the Base of Seismic Resistant Reinforced Concrete Columns Retrofitted with FRPs—3D Finite Element Analysis. *Fibers* **2022**, *10*, 107. [CrossRef]
50. Hany, N.F.; Hantouche, E.G.; Harajli, M.H. Finite Element Modeling of FRP-Confined Concrete Using Modified Concrete Damaged Plasticity. *Eng. Struct.* **2016**, *125*, 1–14. [CrossRef]

Disclaimer/Publisher's Note: The statements, opinions and data contained in all publications are solely those of the individual author(s) and contributor(s) and not of MDPI and/or the editor(s). MDPI and/or the editor(s) disclaim responsibility for any injury to people or property resulting from any ideas, methods, instructions or products referred to in the content.